ARTICLE   OPEN

Check for updates

The importance of the image forces and dielectric environment in modeling contacts to two-dimensional materials

Madhuchhanda Brahma[1], Maarten L. Van de Put[1], Edward Chen[2], Massimo V. Fischetti [1] and William G. Vandenberghe [1✉]

The performance of transistors based on two-dimensional (2D) materials is affected largely by the contact resistance due to high Schottky barriers at the metal-2D-material interface. In this work, we incorporate the effect of surrounding dielectrics and image-force barrier-lowering in calculating the resistance of Schottky edge-contacts between a metal and a transition-metal dichalcogenide (TMD) thin layer. The electrostatic potential is computed by solving the Poisson equation numerically. The transmission probability is computed using the Wentzel–Kramers–Brillouin (WKB) approximation using the full-band density of states obtained from density functional theory (DFT). The effect of the image force is obtained analytically using the Coulomb kernel of a point charge with boundary conditions appropriate to the geometry we have considered. We find that the image-force barrier-lowering (IFBL) in edge-contacts is determined mainly by the dielectric permittivity of the surrounding oxide. We find that low-κ surrounding dielectrics are crucial for obtaining low resistance monolayer-TMD edge-contacts. Our results show metal-to-n(p)-type MoS$_2$ (WSe$_2$) edge-contacts with SiO$_2$ as top and bottom insulators, a doping concentration $> 1 \times 10^{13} \text{cm}^{-2}$ and a metal work-function < 5.1 eV (> 4.6 eV) result in a contact resistance as low as $50 \, \Omega \cdot \mu\text{m}$.

INTRODUCTION

In scaled Si-based field-effect transistors (FETs), reducing the thickness of the Si body is accompanied by severe short-channel effects which degrade device performance. In order to extend the complementary metal-oxide-semiconductor (CMOS) technology road-map beyond Moore's law, atomically thin 2D materials, such as graphene, hexagonal boron nitride (h-BN), transition metal dichalcogenides (TMDs), such as MoS$_2$, WS$_2$, MoSe$_2$, WSe$_2$, and MoTe$_2$, silicene, phosphorene[1–5], are being studied extensively as candidates for nanoelectronic and optoelectronic applications[2,6–11].

A low contact resistance is essential for a high on-current in FETs. However, metal-TMD contacts are characterized by high Schottky barriers[7,12–16] which make it difficult to achieve silicon-like contact resistance (<0.2 k$\Omega \cdot \mu$m) and severely limit the drive current in such devices. Semiconducting MoS$_2$, one of the widely studied TMDs considered as channels in 2D FETs, shows contact resistance values usually higher than 1 k$\Omega \cdot \mu$m[12–15]. One of the lowest contact resistance values reported for multilayer MoS$_2$ FETs is 0.54 k$\Omega \cdot \mu$m with an on-current of 830 µA/µm at 300 K[17]. Phase-engineered metallic 1T MoS$_2$, when used as electrode, demonstrated significantly low contact resistance such as $0.2 - 0.3$ k$\Omega \cdot \mu$m with an on-current of 100 µA/µm for multilayer, and 0.2 k$\Omega \cdot \mu$m with on current of 110 µA/µm for monolayer MoS$_2$ channel[18,19]. n-doping of MoS$_2$ by AlO$_x$ has also resulted in FETs with Au contacts and monolayer MoS$_2$ as channel, exhibiting a resistance as low as 0.48 k$\Omega \cdot \mu$m with an on-current 700 µA/µm [20]. To date, the lowest contact resistance reported is 0.13 k$\Omega \cdot \mu$m, which was obtained by using semi-metal contact (semi-metallic bismuth on MoS$_2$)[21]. However, low melting temperature (250℃) limits its application. Another TMD that has been of interest due to its p-type behavior is WSe$_2$ which has been shown to exhibit contact resistance as low as 0.3 k$\Omega \cdot \mu$m with an on-current of 300 µA/µm [22]. In these studies, the top-contact configuration had been used where a 3D bulk metal sits directly on top of the TMD

semiconducting layer. Apart from top contacts, edge-contact TMDs are also being studied. Cui et al. demonstrated h-BN encapsulated MoS$_2$ thin layers in contact with graphene-metal edge contacts[23]. Choi et al. studied a multilayer hBN-encapsulated MoS$_2$ edge-contact on a SiO$_2$/Si substrate[24], whereas Yang et al. showed fermi-level depinning in plasma-etched MoS$_2$ metal edge-contacts[25]. Cheng et al. demonstrated how they utilized in-situ etching for contact metal deposition and obtained a contact resistance of 30 k$\Omega \cdot \mu$m at a channel electron density of 1.2×10^{12} cm^{-2}[26]. Recently, a contact resistance as low as 27.8 k$\Omega \cdot \mu$m has been reported for edge-contacts with contact metal Ti-Au and monolayers of MoS$_2$ encapsulated by h-BN, while retaining an on-current comparable to what is obtained using top-contacts (>50 µA/µm)[27].

Although there has been an extensive experimental investigation of the contact geometry in 2D FETs, theoretical studies are limited. Some of the studies have employed first-principles and transport calculations using non-equilibrium Green's functions, to investigate the electronic structure at the interface of both top and edge-contacts and to extract the Schottky barrier heights[28–30], whereas other study investigated dominant current mechanisms in vertical transport through TMD hetero-structures[31]. A study incorporating ab initio quantum-transport simulations to predict the influence of transfer length and interfacial oxide on the carrier injection process through metal-TMD contacts has also been recently reported[32]. Other theoretical studies on the resistance of metal-TMD contacts calculate the electrical resistance for a simplified problem without incorporating the effect of the Schottky barrier[33,34]. However, all these studies exclude the effect of the surrounding dielectrics, an effect which is shown to be important in such 2D geometry[35,36]. Another critical effect that controls the properties of contacts is the barrier lowering caused by the image force which has not received any attention for 2D materials.

[1]Department of Materials Science and Engineering, The University of Texas at Dallas, 800 W. Campbell Rd., Richardson, TX 75080, USA. [2]Corporate Research, Taiwan Semiconductor Manufacturing Company Ltd., 168, Park Ave. II, Hsinchu Science Park, Hsinchu 300-75, Taiwan. ✉email: william.vandenberghe@utdallas.edu

In this work, we intend to focus on the importance of the surrounding dielectric and image-force barrier-lowering on the contact resistance of metal-TMD edge-contacts. Our model assumes an ideal Schottky interface ignoring a possible change of the atomic morphology of the interface and treats the injection mechanism in a simplified way. We have preferred this geometry for the computational simplicity it affords and for its presumable advantage of not involving tunneling across a van der Waals gap. Despite this restriction, our results regarding the beneficial role of high doping and low-κ insulators should apply to more general contact geometries, such as top-contacts. We use the full-band density of states of the TMDs obtained from density functional theory (DFT), and the WKB approximation to calculate the transmission probability through the Schottky barrier at the metal-TMD interface, including also the important effect of image-force barrier-lowering on the TMD potential. However, our ultimate goal consists in emphasizing the major effects played by the Schottky barrier, by its reduction due to the image potential and, most notably, by the surrounding dielectrics (due to the monolayer nature of the semiconductor), effects that remain important, if not even dominant, regardless of the models employed to treat the interface. Specifically, as a simple consequence of the Poisson equation, our results emphasize the role of a high doping concentration and a low surrounding dielectric permittivity to obtain the best contact resistance.

We organize the paper as follows: We first show our results, discussing the values of the contact resistance we have obtained, and the role played by the different choices of the parameters we have used. Next, we describe the numerical and mathematical approach we have used. Finally, we draw our conclusions.

RESULTS AND DISCUSSION

Edge-contact geometry and calculation of contact resistance

In Fig. 1a, b, we illustrate the geometry we consider: A semi-infinite TMD monolayer "sandwiched" between very thick top and bottom dielectrics ($t_{dielectric} \gg t_{2D}$), with a metal contact on the side. We consider two types of monolayer TMDs namely MoS$_2$ and WSe$_2$ as the channel material. We first present n-type monolayer MoS$_2$ to shed light on our main findings. We consider an infinitely wide device and assume translational invariance along the y direction. The transport is along the x direction. We consider the same dielectric material as top and bottom insulators, either SiO$_2$ or HfO$_2$. We use anisotropic dielectric permittivity for the TMDs[37]. We consider a piece-wise homogeneous isotropic dielectric permittivity for the top and bottom insulators, $3.9\epsilon_0$ and $25\epsilon_0$ for SiO$_2$ and HfO$_2$, respectively.

We have calculated the transmission probability through the Schottky barrier invoking the WKB approximation with an electrostatic potential calculated accounting also for the effect of the image-force barrier-lowering. To obtain the electrostatic potential in the TMD, we solve self-consistently the Poisson equation using the finite elements-based package, FEniCS[38,39] over the 2D cross-section shown in Fig. 1b. We assume that the contact clamps the potential at the metal-TMD/metal-oxide interface; that is, the metal is assumed to be a region of constant potential. More details on the computational approach for calculating the contact resistance is available in the "Methods" section.

Importance of the surrounding dielectric

Figure 2 shows our main result, the calculated contact resistance as a function of doping concentration, in bulk MoS$_2$ and edge-contact geometry of MoS$_2$ monolayers (n-doped) with either SiO$_2$ (MoS$_2$/SiO$_2$) or HfO$_2$ (MoS$_2$/HfO$_2$) as top and bottom insulators. We see that increasing the doping concentration reduces the contact resistance, a trend that is consistent with what is observed in
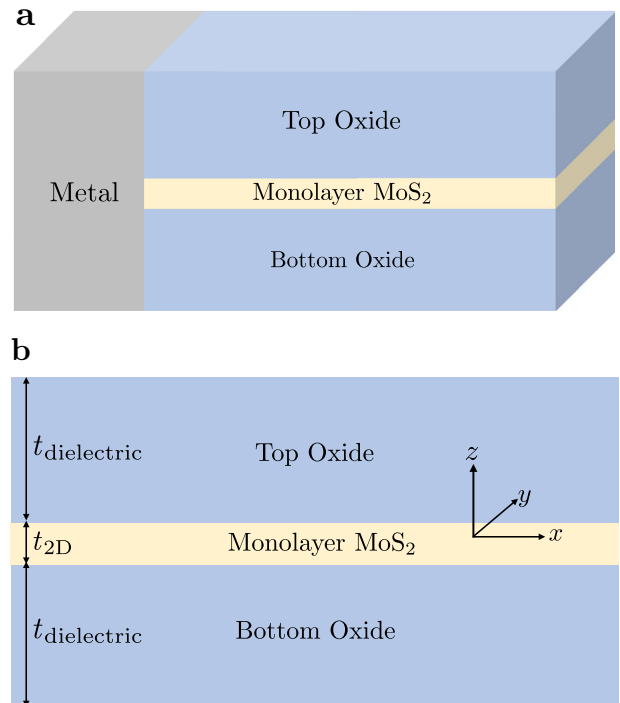

Fig. 1 Schematic of an edge-contact. a Edge-contact geometry considered in our model. **b** 2D cross-section of the edge-contact geometry (metal not shown). The middle layer is monolayer MoS$_2$ "sandwiched" between infinitely-thick top and bottom oxides ($t_{dielectric} \gg t_{2D}$, where t_{2D} and $t_{dielectric}$ denote the thickness of the TMD and oxide layers, the values of which are 0.62 nm and 50 nm, respectively). The Poisson equation is solved over this 2D cross-section.
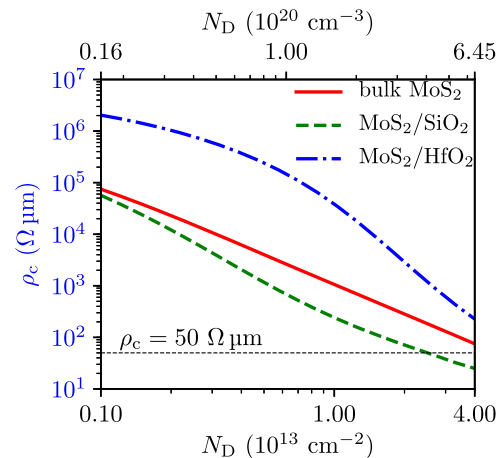
Fig. 2 Contact resistance of monolayer MoS$_2$ edge-contact. Calculated contact resistance vs. doping concentration for bulk and monolayer MoS$_2$ edge contacts at a Schottky barrier height of 0.3 eV. MoS$_2$ monolayers "sandwiched" between SiO$_2$ or HfO$_2$ are labeled as MoS$_2$/SiO$_2$ and MoS$_2$/HfO$_2$, respectively. The bottom and top x axes denote the 2D and bulk doping concentration in MoS$_2$, respectively. The lowest contact resistance is achieved for MoS$_2$ with top and bottom insulators as SiO$_2$.

metal-bulk-semiconductor contacts. Interestingly, we find that in the presence of a low-κ surrounding dielectric, such as SiO$_2$, monolayer MoS$_2$ presents a lower contact resistance than its bulk counterpart. Contact resistances calculated excluding the effect of IFBL are shown for each case of the surrounding dielectric in Supplementary Fig. 1 of the Supplementary Information. We show
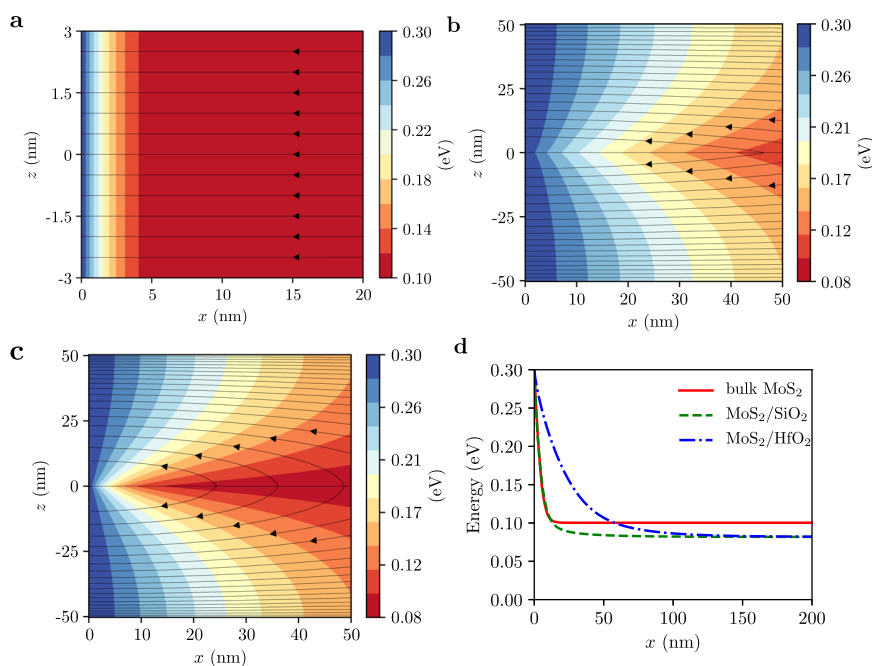
Fig. 3 Potential energy. Contour plots of potential energy with electric field lines for **a** bulk MoS_2, monolayer MoS_2 surrounded by **b** SiO_2 and **c** HfO_2, and **d** potential energies obtained from 1D cuts of the 2D potential energy along the center ($z = 0$) of the monolayer, at a Schottky barrier height of 0.3 eV and doping concentration of 1×10^{12} cm^{-2}.

a similar plot with the contact resistance of p-WSe_2 in Supplementary Fig. 2 of the Supplementary Information. However, it should be noted that barrier-lowering due to image force, is a physical phenomenon, arising when a metal encounters a semiconductor, an effect that is always present in metal contacts. The improvement in contact resistance in monolayer MoS_2 (and WSe_2) due to barrier-lowering is the largest, ~40 times (~30 times), when the surrounding dielectric is SiO_2 compared to HfO_2, which gives ~5 times improvement, as illustrated in Supplementary Figs. 1 and 2 of the Supplementary Information. We also find that to achieve a contact resistance of $50 \, \Omega \cdot \mu m$, monolayer MoS_2 and WSe_2 require to be doped at a concentration $>1 \times 10^{13}$ cm^{-2}. Thus, from Fig. 2 it is apparent that the surrounding dielectrics affect very strongly the electrostatic behavior of such 2D geometries.

While a direct comparison of our results to experiments is beyond the scope of this work, below we discuss some of the experimental studies. Values of the contact resistances reported below were extracted and reported by Parto et al.[30]. A multilayer hBN-encapsulated MoS_2 edge contact on a SiO_2/Si substrate[39] was studied by Choi et al. where a contact resistance of 6×10^2 k$\Omega \cdot \mu$m was obtained at a channel electron density of 2×10^{12} cm^{-2} with Mn as contact metal[30]. Chai et al. studied a monolayer MoS_2 edge-contact (encapsulated by hBN and SiO_2 as gate dielectric)[40], obtaining a contact resistance of 3×10^3 k$\Omega \cdot \mu$m at a channel electronic density of 4×10^{12} cm^{-2} and Sc/Ni contact metal[30]. h-BN encapsulated monolayer MoS_2 edge-contact on Si/SiO_2 substrate studied by Moon et al.[41] had a contact resistance of 10^3 k$\Omega \cdot \mu$m at an electron density of 4×10^{12} cm^{-230}. Furthermore, from Fig. 2 in ref. [30], we find that the values of the edge-contact resistance in monolayer MoS_2 range from 40 k$\Omega \cdot \mu$m to 4×10^3 k$\Omega \cdot \mu$m as the electron density spans the range 10^{12} cm^{-2} to 2×10^{13} cm^{-2}. These values are larger than our calculated values. Note that in our model we ignore the complexities of the interface between the metal and TMD, neglecting, for example, the nature of the chemical bond, the effects of disorder, of interface polarization, of changes in the band offset, of Fermi-pinning, and of phonon scattering. This allows us to treat the contact as an abrupt heterostructure and adopt the

idealized mesoscopic approximation of assuming that the band structure of the bulk metal changes to the TMD band-structure at the point of contact. More advanced calculations are therefore needed to predict accurately the absolute contact resistance. Despite these limitations, our work highlights the importance of the image-force barrier lowering and the surrounding dielectric, effects that are largely ignored in more advanced calculations. We will show that these electrostatic effects, which rely only on the Coulomb interaction and geometry, have a surprisingly strong influence on the contact resistance and even drive the design of the dielectric layers around the metal-TMD contact.

Considering the physics that governs the contact, the dielectric response of the surrounding material enters in two ways. First, the length of the depletion region in the 2D material is affected by the surrounding dielectric. Second, the image-force barrier-lowering effect, resulting from the attractive force emerging from the metal, becomes stronger with a surrounding dielectric material having a lower dielectric constant. The first effect is illustrated in Fig. 3 and the second in Fig. 4.

Depletion width

Figure 3a–c shows the contour maps of the 2D potential energy with electric field lines whereas Fig. 3d shows the potential energy, obtained as 1D cut of the 2D potential energy, along the center of the MoS_2 channel. From Fig. 3a–c, we find that the electric field is screened more effectively in bulk, compared to 2D MoS_2 monolayers. Monolayer TMDs are subject to strong fringing fields permeating the surrounding dielectric. As a result, a high-κ dielectric such as HfO_2 reduces screening. A direct consequence of weaker screening is a larger depletion width as shown in Fig. 3d. The potential energy in bulk MoS_2 falls sharply with the smallest depletion width. 2D MoS_2 surrounded by HfO_2 exhibits a larger depletion width in contrast to SiO_2. A larger depletion width results in a thicker tunneling barrier and, therefore reduces the transmission probability through the Schottky barrier at the metal-TMD interface. This is one of the reasons that we see higher contact resistance in MoS_2 surrounded by high-κ dielectric such as HfO_2.
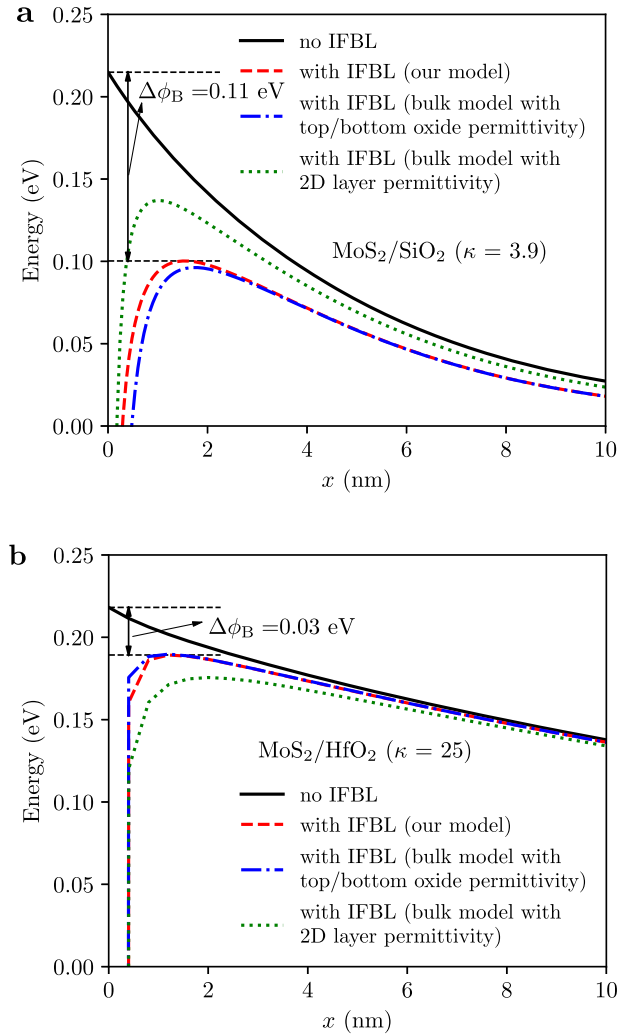
Fig. 4 Image-force barrier-lowered potential energy. Potential energy along the center of the monolayer calculated ignoring image-force barrier-lowering (black solid line), the "correct" 2D solution (red dashed line) using our model, and the bulk model for the barrier lowering (blue dashed-dot and green dotted lines, using TMD and insulator permittivity, respectively), at a Schottky-barrier height of 0.3 eV and a doping concentration $N_D = 1 \times 10^{12}$ cm^{-2}, assuming the same top and bottom dielectric materials which are **a** SiO$_2$ and **b** HfO$_2$. $\Delta\phi_B$ denotes the barrier lowering.

Image-force barrier lowering

The second effect, the image-force barrier-lowering (IFBL), consists in the reduction of the effective barrier height due to the presence of image charges inside the metal contact. The metal region must maintain a constant potential as an electron tunnels through the Schottky barrier. The role played by the IFBL is illustrated in Fig. 4 which shows the potential energy as in Fig. 3, but now accounting for the IFBL at a fixed doping concentration in the two extreme cases of SiO$_2$ (Fig. 4a) and HfO$_2$ (Fig. 4b). The magnitude of barrier lowering is the difference between the peak of the no-IFBL and IFBL potential energies (shown by the arrow in Fig. 4). We observe that at a low doping concentration ($N_D = 1 \times 10^{12}$ cm^{-2}), the conventional (as used in bulk semiconductor contacts) barrier-lowered potential, $1/(16\pi\epsilon x)$ [42], ϵ being the permittivity of the surrounding dielectric, describes the barrier lowering in the contact quite well (it only underestimates the barrier by 0.0039 eV and 0.0005 eV in MoS$_2$/SiO$_2$ and MoS$_2$/HfO$_2$, respectively.) However, as the doping concentration increases and tunneling occurs closer to the contact, the conventional bulk
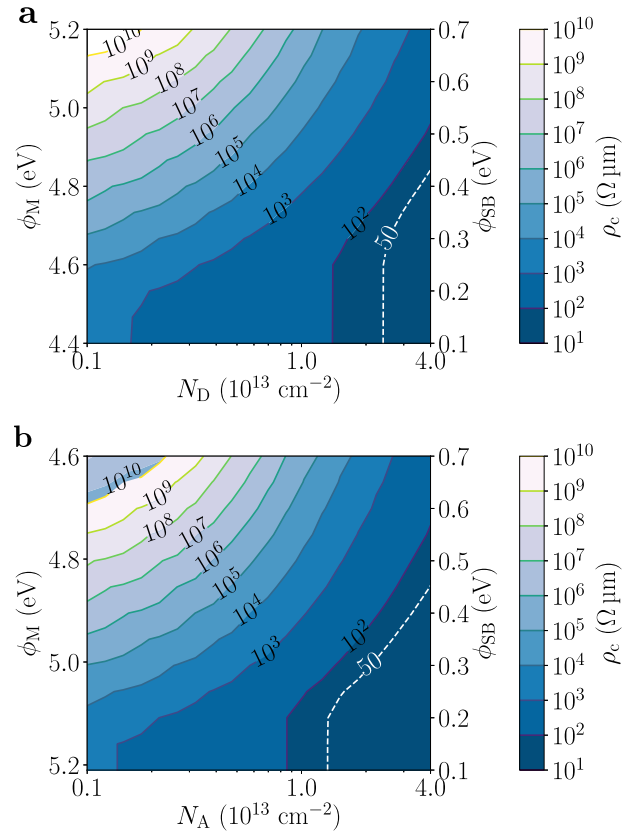
Fig. 5 Contact resistance map. Contour plot of contact resistance as function of metal work function and Schottky barrier-height in **a** n-type MoS$_2$ and **b** p-type WSe$_2$, with top and bottom insulator as SiO$_2$.

model fails to capture the barrier lowering accurately (see "Image potential" in "Methods" section for more details). The thickness of the barrier plays a particularly strong role, and it is also strongly modulated by the dielectric constant of the surrounding insulator. In Fig. 4, we observe that barrier narrowing is larger in MoS$_2$/SiO$_2$ than MoS$_2$/HfO$_2$, in addition to barrier lowering. These improve the tunneling and thermionic emission, respectively, and overall lead to a decrease in contact resistance.

Monolayer n-MoS$_2$ and p-WSe$_2$ edge-contact

In, Fig. 5a, b, we show the map of contact resistance as a function of metal work-function, Schottky barrier-height and doping concentration, for n-type MoS$_2$ and p-type WSe$_2$ with SiO$_2$ as top and bottom insulators. The x axis denotes the doping concentration whereas the left and right y axes denote the metal work-function and the Schottky barrier-height, respectively. The electron affinities (χ) of MoS$_2$ and WSe$_2$, determined from DFT calculations are 3.96 eV and 3.36 eV, respectively. Schottky barrier-height in n-type semiconductor is calculated as $\phi_{Bn} = \phi_M - \chi$ and in p-type as $\phi_{Bp} = \chi + \frac{E_g}{e} - \phi_M$, where ϕ_M is the metal work-function and E_g is the energy band-gap which is found to be 1.76 eV in monolayer WSe$_2$ from DFT calculation. Therefore, as the metal work-function increases, the Schottky barrier-height increases in n-type and decreases in p-type materials.

In order to obtain a contact resistance as low as 50 Ω μm, both structures require a doping concentration $> 1 \times 10^{13}$ cm^{-2}. However, n-type MoS$_2$ and p-type WSe$_2$ require metals with work-function < 5.1 eV and > 4.6 eV, respectively. These contour plots can be viewed as a guideline for the selection of contact metal and doping concentration for various edge-contact 2D materials,

thereby narrowing down the material and design selection space for expensive experimental device fabrication.

WKB vs. NEGF

We use a finite elements solver to solve the Poisson equation and the WKB approximation to calculate the contact resistance. To understand why we opt for the Poisson-WKB approach instead of the atomistic Non-Equilibrium Green's function (NEGF) approach used by other recent studies on contacts[30], we provide an estimate of the depletion length that needs to be considered. For the lowest doping concentration, 10^{12} cm^{-2}, the highest dielectric constant dielectric, HfO$_2$, and the highest Schottky barrier $\phi_{SB} = 0.7$ V, the 2D depletion width is estimated as $\phi_{SB}\pi\epsilon/((4)eN_D) = 219$ nm[36]. Even at high doping concentration, a relatively large simulation domain, much larger than typically used in DFT, is still required. Dealing with simulation domains on this order of magnitude makes the use of atomistic NEGF codes[43–45] computationally prohibitive whereas solving the Poisson equation and using the WKB approximation can yield an accurate value of the contact resistance. Moreover, to match our results, one must employ hybrid DFT functionals and include spin-orbit coupling. The large number of k-points required to reach convergence for the calculation of the current adds to the computational expense. Moreover, only results obtained ignoring image-force barrier lowering could be compared with the DFT + NEGF code.

To assess the accuracy of the WKB approximation, we implement an effective mass NEGF calculation[46] and compare with the WKB. In Fig. 6, we show the plot of the contact resistances calculated using both the WKB approximation and the NEGF, at a Schottky barrier height of 0.3 eV for MoS$_2$ surrounded by SiO$_2$ or HfO$_2$. It should be noted, that the NEGF calculations use a full effective-mass Hamiltonian whereas the WKB calculations are done using the band structure from DFT. We treat both 'ideal' and

'metal' contact in our NEGF model. The details of the calculation are discussed in the 'Methods' section. If we compare the contact resistances obtained from the WKB approximation with those from the 'ideal' contact-NEGF formalism, we see that the values are very close, with the WKB approximation resulting in a slight overestimation of the conductance with respect to the NEGF. Moreover, we find that the contact resistances calculated by the 'metal' contact-NEGF formalism depends on the self-energy or the coupling strength. The stronger the coupling, the better the contact resistance. However, based on this NEGF estimate, it appears that by using SiO$_2$ rather than HfO$_2$ results in a more noticeable improvement of the contact resistance than what is obtained by increasing the bond strength by a factor 20. Therefore, the main conclusion of our work (namely: low-κ dielectrics are better candidates to obtain low resistance contacts in 2D materials), still holds.

In summary, we have simulated the transmission through metal-2D-materials edge-contacts with Schottky barrier at their interface, using the WKB approximation, and DFT density of states, and obtained the contact resistance. We have shown how the Schottky barrier height, the doping concentration, and the surrounding dielectric environment largely control the electrostatics in 2D devices by considering cases with both low and high-κ oxides.

The primary finding of our study is that low-κ top and bottom insulators surrounding monolayer TMDs result in a low contact resistance, outperforming bulk TMD contacts, thanks to a smaller depletion length and a higher image-force barrier-lowering. We find that, contrary to the bulk case, image-force barrier-lowering in edge-contact 2D devices is determined by the dielectric permittivity of both the surrounding oxide and the TMD. We have also compared the contour plots of contact resistance in two of the most widely studied TMD materials, n-type MoS$_2$ and p-type WSe$_2$ as a function of metal work-function and Schottky barrier-height, which can be considered as guidelines for the fabrication of realistic edge-contact 2D devices.

METHODS

DFT calculation

We performed DFT calculations for bulk MoS$_2$, monolayer MoS$_2$ and monolayer WSe$_2$, using the Vienna Ab initio Simulation Package (VASP)[47–50]. We first ran geometry optimization until the maximum force on every atom dropped below 0.01 eV/Å. We employed the generalized gradient approximation (GGA) with the projector-augmented wave (PAW) method[51] using the Perdew-Burke-Ernzerhof (PBE) exchange-correlation functional[52]. A large vacuum space of 30Å was used along the z direction to avoid interaction between successive layers. We used the DFT-D3 dispersion correction of Grimme[53] to describe van der Waals interactions and accurately calculate the interlayer distance. Thereafter, we used the relaxed structure to perform electronic calculations.

For monolayer TMDs, we first calculated the band structure on a coarse mesh followed by interpolation on a finer mesh by using Maximally Localized Wannier Functions (MLWF) generated by the Wannier90 code[54]. The interpolation preserves the accuracy of the DFT calculations at a lower computational cost. We used the Heyd-Scuseria-Ernzerhof (HSE06) hybrid functional[55] with spin-orbit coupling and an electronic convergence of 10^{-6} eV. To compute the band structure we sampled the Brillouin zone with a Γ-centered $8 \times 8 \times 1$ and $8 \times 8 \times 4$ k-mesh in monolayer and bulk TMDs respectively. We used the d and p orbitals of the metal and chalcogenide atoms as Wannier projectors to interpolate the DFT band structure on a denser $100 \times 100 \times 1$ k-mesh in monolayer TMDs, which was then utilized in calculating the transmission probability.
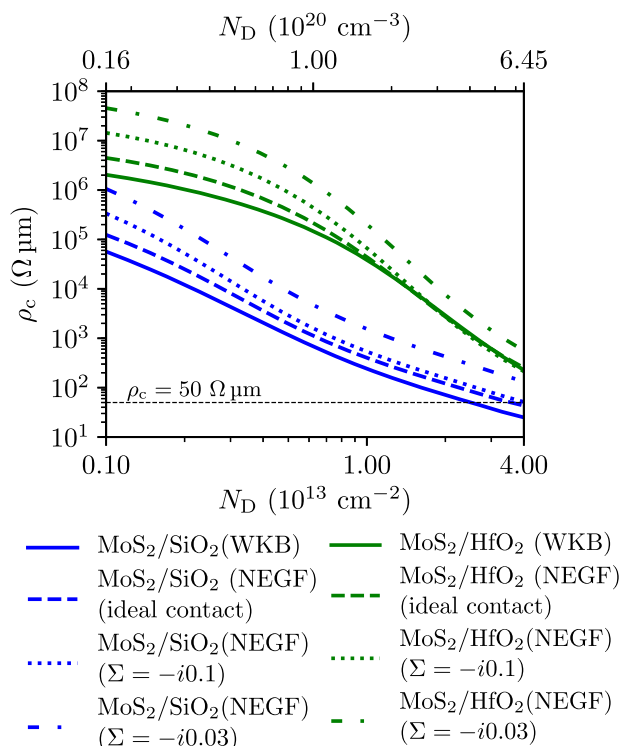
Fig. 6 Contact resistance with WKB and NEGF. Contact resistance vs. doping concentration for MoS$_2$ edge-contacts at a Schottky barrier height of 0.3 eV using WKB and NEGF. Values obtained with WKB approximation show a good match with those calculated by NEGF with "ideal" contacts.

The Poisson equation

We obtained the potential inside the TMD layer by solving the 2D Poisson equation (in the (x, z) plane) self consistently with the charge determined from the full-band density of states. The 2D Poisson equation in a metal-n type semiconductor contact is:

$$\nabla \cdot [\overline{\epsilon}(x,z)\nabla V_{\text{dep}}(x,z)] = e[N_{\text{D}}(x,z) - n_0(x,z)] \quad (1)$$

where $N_{\text{D}}(x,z)$ and $n_0(x,z)$ are the n-type doping concentration and electron carrier density, respectively, $V_{\text{dep}}(x,z)$ is the 2D depletion potential, and $\overline{\epsilon}(x,z)$ is the dielectric permittivity tensor. The in-plane dielectric constant values used for monolayer MoS$_2$, WSe$_2$ and bulk MoS$_2$ are $15.5\epsilon_0, 15.6\epsilon_0$ and $15.9\epsilon_0$[37], whereas the out-of plane values are $6.2\epsilon_0, 7.4\epsilon_0$ and $6.9\epsilon_0$, respectively, with ϵ_0 being the vacuum permittivity. We calculated the electron density from the DFT band structure as:

$$n_0 = 2\sum_n \int f[E_n(\mathbf{k})]\frac{d\mathbf{k}}{(2\pi)^2} \quad (2)$$

where, $E_n(\mathbf{k})$ denotes the full-band dispersion obtained from DFT, n is the band index for the monolayer TMD, and $\mathbf{k}$ is the two-dimensional wave-vector.

The simulation domain for solving the 2D Poisson equation is a rectangle (see Fig. 1) with a TMD layer "sandwiched" between 50 nm-thick oxide layers. The thickness of the TMD layer was determined from the relaxed geometry obtained with DFT, and was found to be 0.62 nm and 0.65 nm for monolayer MoS$_2$ and monolayer WSe$_2$, respectively. We used Dirichlet boundary conditions at the metal contact and Neumann boundary conditions on the other sides (thus ignoring any effect of a gate bias). The size of the simulation domain is 100.62 nm × 400 nm. The top and bottom oxide thickness is substantially greater than the thickness of the 2D layer to ensure minimal impact of the Neumann boundary conditions on the electrostatics of the 2D layer[36,56].

We solved Eq. (1) numerically by finite-elements in FEniCS[38,39]. We used the built-in mesh generator of FEniCS to generate a structured mesh of 1000 × 250 elements throughout the computational domain and further refined it at the metal-semiconductor interface to accurately capture the high electric fields near the metal.

Contact resistance

Owing to the very high density of states in the metal and high Schottky barrier-height, we assumed that the transmission probability is governed only by the states in the semiconducting monolayer TMD. We also conserve parallel momentum, which results from our assumption of translational invariance along the y direction. We calculated the contact resistance for edge-contact 2D monolayers as the inverse of ballistic conductance modulated by the probability of the carriers injected through a Schottky barrier[57], using the following:

$$\frac{1}{\rho_c} = \int_{-\infty}^{\infty} \frac{2e^2}{h}\left\{\int\left[\sum_n\left(\int\delta[E - E_n(k_y)]dE_n(k_y)\right)T_n(k_y,E)\right]\frac{dk_y}{(2\pi)}\right\}\left|\frac{-\partial f(E)}{\partial E}\right|dE \quad (3)$$

$$= \int_{-\infty}^{\infty} \frac{2e^2}{h}\left\{\int\left[\sum_n M_n(k_y,E)T_n(k_y,E)\right]\frac{dk_y}{2\pi}\right\}\left|\frac{\partial f(E)}{\partial E}\right|dE \quad (4)$$

where ρ_c denotes the contact resistance, e is the electronic charge, h is Planck's constant, n is the band index for the monolayer TMD, k_y is the parallel wave-vector, and $f(E)$ is the Fermi-Dirac distribution function. $E_n(k_y)$ was calculated from the full band DFT energy band-dispersion. $T_n(k_y, E)$ is the transmission probability as a function of energy E and k_y. $M(k_y, E)$ denotes the number of conducting channels at the energy of interest, and would result in the ballistic conductance if the WKB integral was not present. We calculated Eq. (4) numerically from the energy band dispersion obtained with DFT.

Following the WKB approximation, we have the transmission probability, $T(k_y, E) < 1$, for carriers tunneling through the Schottky barrier, and $T(k_y, E) = 1$, for carriers injected over the top of the barrier. The transmission probability was calculated as:

$$T_n(k_y,E) = \exp\left(-2\int_{x_{\min}}^{x_{\max}}\sqrt{\frac{2m_n^*(k_y)}{\hbar^2}\left[E - U(x) - E_{n,\min}(k_y)\right]}\,dx\right) \quad (5)$$

where $m_n^*(k_y)$ is the tunneling effective-mass computed numerically using finite difference from the DFT energy band structure, $x_{\min}$ and $x_{\max}$ denote the start and end of the depletion region, E is the energy of the carriers, and $E_{n,\min}(k_y)$ is the band-edge obtained from the DFT energy band structure. $U(x)$ is the barrier-lowered potential energy where $U(x) = U_{\text{dep}}(x) + U_{\text{image}}(x)$. $U_{\text{dep}}(x)$ is the Schottky depletion potential energy which was obtained from the 1D cut of the 2D depletion potential at the center of the monolayer TMD along the transport direction. $U_{\text{image}}(x)$ is image-force potential energy. The potential energy is related to the electrostatic potential by the relation $U_{\text{dep(image)}} = -eV_{\text{dep(image)}}$.

Image potential

In order to calculate how the image force lowers the height of the Schottky barrier in our 2D geometry, we first computed the Coulomb kernel for a charged particle somewhere in the middle of the monolayer shown in Fig. 7. The effect of the metal was ignored in this first step and accounted for next by the method of images. The equation for the Green's function of the Poisson equation in our geometry is:

$$\nabla \cdot [\epsilon(\mathbf{r})\nabla V_{\text{image}}(\mathbf{r})] = \delta(\mathbf{r}). \quad (6)$$

where $\mathbf{r}$ is the three-dimensional position vector, $V_{\text{image}}(\mathbf{r})$ stands for the image potential, $\epsilon(\mathbf{r})$ is the dielectric permittivity, and $\delta(\mathbf{r})$ is the point charge source.

We considered circular symmetry and applied the Hankel or Fourier-Bessel transform of zeroth order on Eq. (6). We used the relation, $\hat{V}_{\text{image}}(Q) = \int_0^\infty rV_{\text{image}}(r)J_0(Qr)dr$, (where, Q is the
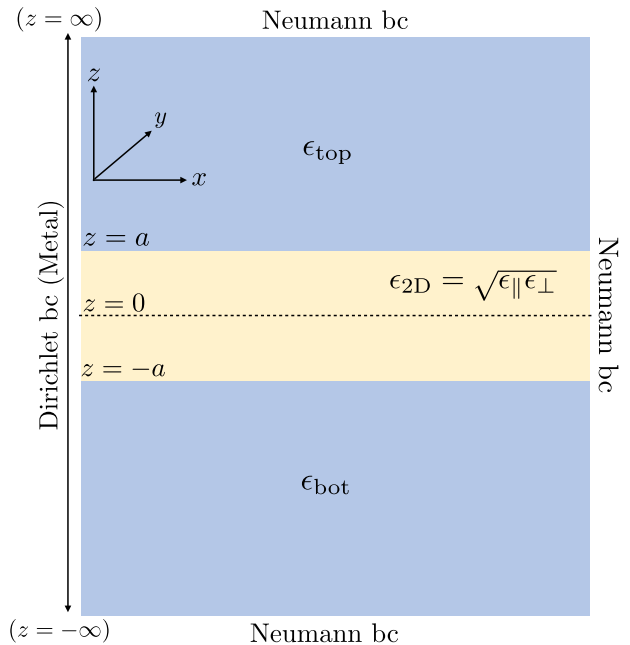
Fig. 7 Dielectric environment for the image force. Schematic of the structure where we compute the Coulomb kernel with a point charge located at $z = 0$. The top and bottom oxides have a homogeneous isotropic permittivity, whereas the middle (2D) semiconductor has an anisotropic permittivity.
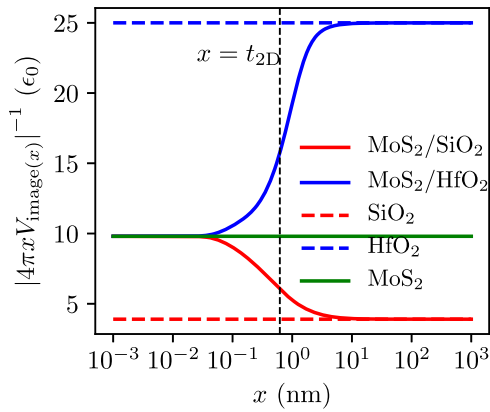
Fig. 8 Image-force barrier potential versus position. $|4\pi x V_{image}(x)|^{-1}$ plotted as a function of the distance from the metal-TMD interface in MoS_2/SiO_2 (our model), MoS_2/HfO_2 (our model), and using the conventional bulk model with oxide permittivity (labeled as SiO_2 and HfO_2) or TMD permittivity (labeled as MoS_2). The quantity $|4\pi x V_{image}(x)|^{-1}$ can be thought of as a "position-dependent dielectric constant". Beyond 1 nm, the dielectric constant of the environment determines the image potential.

transformed Hankel coordinate and is reciprocal to r, and J_0 is the Bessel function of the first kind of order zero), to derive the following partial differential equation:

$$\epsilon_\perp \frac{\partial^2 \hat{V}_{image}(Q,z)}{\partial z^2} + \epsilon_\parallel Q^2 \hat{V}_{image}(Q,z) = \delta(z) \quad (7)$$

where $\epsilon_\perp$ is the out-of plane dielectric permittivity and $\epsilon_\parallel$ is the in-plane dielectric permittivity of the 2D layer.

The boundary conditions for the potential are continuity of $\hat{V}_{image}(Q,z)$ and electric displacement ($\epsilon_\perp \frac{d\hat{V}_{image}(Q,z)}{dz}$) at $z = 0$, and $z = \pm a = \frac{t_{2D}}{2}$, $\hat{V}_{image}(Q,z) = 0$ at $z = \pm\infty$ and a discontinuity due to the source at $z = 0$ for $\hat{V}'_{image}(0+) - \hat{V}'_{image}(0-) = \frac{1}{\epsilon_{2D}Q}$. Using these boundary conditions we obtained six linear equations with six unknown coefficients, whose solution is:

$$\hat{V}_{image}(Q,z=0) = -\frac{2e^{2a\beta Q}[\epsilon_{2D}\cosh(a\beta Q) + \epsilon_{bot}\sinh(a\beta Q)][\epsilon_{2D}\cosh(a\beta Q) + \epsilon_{top}\sinh(a\beta Q)]}{\epsilon_{2D}Q[(\epsilon_{2D} - \epsilon_{top})(\epsilon_{bot} - \epsilon_{2D}) + (\epsilon_{2D} + \epsilon_{top})(\epsilon_{2D} + \epsilon_{bot})e^{4a\beta Q}]}$$

$$(8)$$

where, ϵ_{top} and ϵ_{bot} are the top ($z > a$) and bottom ($z < a$) oxide dielectric permittivity, the thickness of the middle 2D layer ($-a < z < a$) is $2a$, $\epsilon_{2D} = \sqrt{\epsilon_\parallel \epsilon_\perp}$ and $\beta = \sqrt{\frac{\epsilon_\parallel}{\epsilon_\perp}}$.

Finally, the real space potential $V_{image}(x)$ at $(x, 0)$ due to the point charge at $(x, z = 0)$ was obtained numerically[58] as the 2D Fourier-Bessel or Hankel transform of Eq. (8) and calculated as:

$$V_{image}(x,0) = \frac{e}{2\pi}\int_0^\infty \hat{V}_{image}(Q,z=0)J_0(xQ)Q\,dQ \quad (9)$$

where, J_0 is the Bessel function of the first kind of order zero.

We then used the method of images to account for the metal contact and to evaluate the image potential energy. It is defined as the (negative) work done to bring a charge e from infinity to a distance x from the metal-2D interface (at a distance $2x$ from the image charge) and is given by:

$$U_{image}(x) = e\int_\infty^x dx' \frac{dV_{image}(2x',0)}{dx'} \quad (10)$$

which equals $\frac{e}{2}V_{image}(2x)$.

Finally, we show in Fig. 8, the plot of $|4\pi x V_{image}(x)|^{-1}$ with respect to x. Here, x denotes the distance of the point charge from the metal-TMD interface, and $V_{image}(x)$ is the calculated image potential for a point charge located in the middle of the MoS_2

monolayer in the presence of different surrounding dielectrics. Asymptotically, we see that at distances much larger than the layer thickness ($x \gg t_{2D}$), the quantity $|4\pi x V_{image}(x)|^{-1}$ matches the dielectric constant of the surrounding oxide, which implies that the barrier-lowered potential behaves as $1/(\epsilon_{dielectric}x)$. On the other hand, when $x \ll t_{2D}$, the 2D-material dielectric constant dominates, as in the bulk case, and the barrier-lowered potential behaves as $1/(\epsilon_{2D}x)$. When $x \approx t_{2D}$, a numerical evaluation is required to obtain the correct result. For $x \gg t_{2D}$, the conventional bulk model[42] (using oxide permittivity) matches the correct solution but fails when $x \ll t_{2D}$.

Calculation of contact resistance using NEGF

We used an effective-mass Hamiltonian to compute the transmission with NEGF formalism. We calculated the effective mass of monolayer MoS_2 along the transport direction x from the DFT band structure using finite differences. We solved the retarded Green's function as a function of k_y and discretized using $\Delta k_y = 2\pi n/(150\,nm)$. We used the same electrostatic potential as in the WKB calculations. The barrier lowered potential needs to be truncated to avoid the singularity at $x = 0$ that occurs when ignoring the self-consistent many-body effects considered in ref. [59]. For simplicity, we just truncated the potential at $U = -1$ eV. We chose a spacing of 0.4 nm to discretize the effective-mass Hamiltonian and 0.003 eV to discretize the energy range. In the WKB approximation, we assumed ideal metal contacts and ignored any band-structure mismatch. However, under the NEGF formalism, we calculated the transmission by considering both 'ideal' and 'metal' contacts. In case of 'ideal' contacts, the contacts were considered as an extension of the device, and the surface Green's function was used to compute the self-energy[46]. On the contrary, the 'metal' contacts were treated using the wide-band limit[60–63], and the contact self-energy was represented as purely imaginary and energy-independent, $\Sigma(E) = -it_0[61,64,65]$, and related to the coupling of the active region (the 2D TMD channel) to the metal via chemical bonds. A stronger coupling strength between the metal and the semiconductor was captured by a higher value of t_0. To illustrate this effect on the contact resistance, we had chosen two values of Σ ($\Sigma(E) = -i0.03$ and $\Sigma(E) = -i0.1$), to capture a bond that is ~20 times weaker and a bond that is ~6 times weaker than the bond in the TMD.

REFERENCES

1. Radisavljevic, B., Radenovic, A., Brivio, J., Giacometti, V. & Kis, A. Single-layer MoS$_2$ transistors. *Nat. Nanotechnol.* **6**, 147 (2011).
2. Wang, Q. H., Kalantar-Zadeh, K., Kis, A., Coleman, J. N. & Strano, M. S. Electronics and optoelectronics of two-dimensional transition metal dichalcogenides. *Nat. Nanotechnol.* **7**, 699 (2012).
3. Miró, P., Audiffred, M. & Heine, T. An atlas of two-dimensional materials. *Chem. Soc. Rev.* **43**, 6537–6554 (2014).
4. Tao, L. et al. Silicene field-effect transistors operating at room temperature. *Nat. Nanotechnol.* **10**, 227 (2015).

5. Liu, H. et al. Phosphorene: an unexplored 2D semiconductor with a high hole mobility. *ACS Nano* **8**, 4033–4041 (2014).

6. Podzorov, V., Gershenson, M., Kloc, C., Zeis, R. & Bucher, E. High-mobility field-effect transistors based on transition metal dichalcogenides. *Appl. Phys. Lett.* **84**, 3301–3303 (2004).

7. Das, S., Chen, H.-Y., Penumatcha, A. V. & Appenzeller, J. High performance multilayer MoS_2 transistors with scandium contacts. *Nano Lett.* **13**, 100–105 (2012).

8. Jariwala, D., Sangwan, V. K., Lauhon, L. J., Marks, T. J. & Hersam, M. C. Emerging device applications for semiconducting two-dimensional transition metal dichalcogenides. *ACS Nano* **8**, 1102–1120 (2014).

9. Jo, S., Ubrig, N., Berger, H., Kuzmenko, A. B. & Morpurgo, A. F. Mono-and bilayer WS_2 light-emitting transistors. *Nano Lett.* **14**, 2019–2025 (2014).

10. Lin, Y.-F. et al. Ambipolar $MoTe_2$ transistors and their applications in logic circuits. *Adv. Mater.* **26**, 3263–3269 (2014).

11. Xia, F., Wang, H. & Jia, Y. Rediscovering black phosphorus as an anisotropic layered material for optoelectronics and electronics. *Nat. Commun.* **5**, 4458 (2014).

12. Das, S. & Appenzeller, J. Where does the current flow in two-dimensional layered systems? *Nano Lett.* **13**, 3396–3402 (2013).

13. Liu, H. et al. Switching mechanism in single-layer molybdenum disulfide transistors: an insight into current flow across Schottky barriers. *ACS Nano* **8**, 1031–1038 (2014).

14. Guo, Y. et al. Study on the resistance distribution at the contact between molybdenum disulfide and metals. *ACS Nano* **8**, 7771–7779 (2014).

15. Allain, A., Kang, J., Banerjee, K. & Kis, A. Electrical contacts to two-dimensional semiconductors. *Nature Mater.* **14**, 1195–1205 (2015).

16. Schulman, D. S., Arnold, A. J. & Das, S. Contact engineering for 2D materials and devices. *Chem. Soc. Rev.* **47**, 3037–3058 (2018).

17. Liu, Y. et al. Pushing the performance limit of sub-100 nm molybdenum disulfide transistors. *Nano Lett.* **16**, 6337–6342 (2016).

18. Kappera, R. et al. Metallic 1T phase source/drain electrodes for field effect transistors from chemical vapor deposited MoS_2. *APL Mater.* **2**, 092516 (2014).

19. Kappera, R. et al. Phase-engineered low-resistance contacts for ultrathin MoS_2 transistors. *Nat. Mater.* **13**, 1128–1134 (2014).

20. McClellan, C. J., Yalon, E., Smithe, K. K., Suryavanshi, S. V. & Pop, E. Effective n-type doping of monolayer MoS_2 by AlO_x. In: *2017 75th Annual Device Research Conference (DRC)*, 1-2 (IEEE, 2017).

21. Shen, P.-C. et al. Ultralow contact resistance between semimetal and monolayer semiconductors. *Nature* **593**, 211–217 (2021).

22. Chuang, H.-J. et al. Low-resistance 2D/2D ohmic contacts: a universal approach to high-performance WSe_2, MoS_2, and $MoSe_2$ transistors. *Nano Lett.* **16**, 1896–1902 (2016).

23. Cui, X. et al. Multi-terminal transport measurements of MoS_2 using a van der Waals heterostructure device platform. *Nat. Nanotechnol.* **10**, 534–540 (2015).

24. Choi, H. et al. Edge contact for carrier injection and transport in MoS_2 field-effect transistors. *ACS Nano* **13**, 13169–13175 (2019).

25. Yang, Z. et al. A Fermi-level-pinning-free 1D electrical contact at the intrinsic 2D MoS_2–metal junction. *Adv. Mater.* **31**, 1808231 (2019).

26. Cheng, Z. et al. Immunity to contact scaling in MoS_2 transistors using in situ edge contacts. *Nano Lett.* **19**, 5077–5085 (2019).

27. Jain, A. et al. One-dimensional edge contacts to a monolayer semiconductor. *Nano Lett.* **19**, 6914–6923 (2019).

28. Cakır, D. & Peeters, F. Dependence of the electronic and transport properties of metal-$MoSe_2$ interfaces on contact structures. *Phys. Rev. B* **89**, 245403 (2014).

29. Jelver, L., Stradi, D., Stokbro, K. & Jacobsen, K. W. Schottky barrier lowering due to interface states in 2D heterophase devices. *Nanoscale Adv.* **3**, 567–574 (2021).

30. Parto, K. et al. One-dimensional edge contacts to two-dimensional transition-metal dichalcogenides: uncovering the role of schottky-barrier anisotropy in charge transport across MoS_2/metal interfaces. *Phys. Rev. Appl.* **15**, 064068 (2021).

31. Zhu, Y., Zhou, R., Zhang, F. & Appenzeller, J. Vertical charge transport through transition metal dichalcogenides–a quantitative analysis. *Nanoscale* **9**, 19108–19113 (2017).

32. Szabó, Á., Jain, A., Parzefall, M., Novotny, L. & Luisier, M. Electron transport through metal/MoS_2 interfaces: edge-or area-dependent process? *Nano Lett.* **19**, 3641–3647 (2019).

33. Mishra, V. & Salahuddin, S. Intrinsic limits to contact resistivity in transition metal dichalcogenides. *IEEE Electron Device Letters* **38**, 1755–1758 (2017).

34. Wickramaratne, D., Zahid, F. & Lake, R. K. Electronic and thermoelectric properties of few-layer transition metal dichalcogenides. *J. Chem. Phys.* **140**, 124710 (2014).

35. Nipane, A., Jayanti, S., Borah, A. & Teherani, J. T. Electrostatics of lateral pn junctions in atomically thin materials. *J. Appl. Phys* **122**, 194501 (2017).

36. Ilatikhameneh, H. et al. Dramatic impact of dimensionality on the electrostatics of PN junctions and its sensing and switching applications. *IEEE Trans. Nanotechnol.* **17**, 293–298 (2018).

37. Laturia, A., Van de Put, M. L. & Vandenberghe, W. G. Dielectric properties of hexagonal boron nitride and transition metal dichalcogenides: from monolayer to bulk. *npj 2D Mater. Appl.* **2**, 1–7 (2018).

38. Alnæs, M. S. et al. The FEniCS Project Version 1.5. Archive of Numerical Software **3**, 100 (2015).

39. Logg, A., Mardal, K.-A. & Wells, G. N. Automated solution of differential equations by the finite element method (Springer, 2012).

40. Chai, Y. et al. Making one-dimensional electrical contacts to molybdenum disulfide-based heterostructures through plasma etching. *Physica Status Solidi* **213**, 1358–1364 (2016).

41. Moon, B. H. et al. Junction-structure-dependent Schottky barrier inhomogeneity and device ideality of monolayer MoS_2 field-effect transistors. *ACS Appl. Mater. Interfaces* **9**, 11240–11246 (2017).

42. Sze, S. M., Li, Y. & Ng, K. K. *Physics of semiconductor devices* (John Wiley & sons, 2021).

43. Smidstrup, S. et al. QuantumATK: an integrated platform of electronic and atomic-scale modelling tools. *J. Phys. Condens. Matter* **32**, 015901 (2019).

44. Van de Put, M. L., Fischetti, M. V. & Vandenberghe, W. G. Scalable atomistic simulations of quantum electron transport using empirical pseudopotentials. *Comput. Phys. Commun.* **244**, 156–169 (2019).

45. Szabó, Á., Rhyner, R. & Luisier, M. Ab initio simulation of single-and few-layer MoS_2 transistors: effect of electron-phonon scattering. *Phys. Rev. B* **92**, 035435 (2015).

46. Datta, S. *Quantum transport: atom to transistor* (Cambridge university press, 2005).

47. Kresse, G. & Hafner, J. Ab initio molecular dynamics for liquid metals. *Phys. Rev. B* **47**, 558 (1993).

48. Kresse, G. & Hafner, J. Ab initio molecular-dynamics simulation of the liquid-metal–amorphous-semiconductor transition in germanium. *Phys. Rev. B* **49**, 14251 (1994).

49. Kresse, G. & Furthmüller, J. Efficient iterative schemes for ab initio total-energy calculations using a plane-wave basis set. *Phys. Rev. B* **54**, 11169 (1996).

50. Kresse, G. & Furthmüller, J. Efficiency of ab-initio total energy calculations for metals and semiconductors using a plane-wave basis set. *Comput. Mater. Sci.* **6**, 15–50 (1996).

51. Kresse, G. & Joubert, D. From ultrasoft pseudopotentials to the projector augmented-wave method. *Phys. Rev. B* **59**, 1758 (1999).

52. Perdew, J. P., Burke, K. & Ernzerhof, M. Generalized gradient approximation made simple. *Phys. Rev. Lett.* **77**, 3865 (1996).

53. Grimme, S., Antony, J., Ehrlich, S. & Krieg, H. A consistent and accurate ab initio parametrization of density functional dispersion correction (DFT-D) for the 94 elements H-Pu. *J. Chem. Phys.* **132**, 154104 (2010).

54. Mostofi, A. A. et al. An updated version of wannier90: a tool for obtaining maximally-localised Wannier functions. *Comput. Phys. Commun.* **185**, 2309–2310 (2014).

55. Heyd, J., Scuseria, G. E. & Ernzerhof, M. Hybrid functionals based on a screened Coulomb potential. *J. Chem. Phys.* **118**, 8207–8215 (2003).

56. Nipane, A., Zhang, Y. & Teherani, J. T. Role of out-of-plane dielectric thickness in the electrostatic simulation of atomically thin lateral junctions. *J. Appl. Phys.* **123**, 214302 (2018).

57. Ravandi, S., Fu, B., Vandenberghe, W. G., Aboud, S. J. & Fischetti, M. V. Pseudopotential-based study of gate leakage and contact resistance beyond the 10 nm node. In 2013 16th International Workshop on Computational Electronics (2013).

58. Murray, S. G. & Poulin, F. J. hankel: A Python library for performing simple and accurate Hankel transformations. *J. Open Source Softw.* **4**, 1397 (2019).

59. Serena, P., Soler, J. & Garcia, N. Self-consistent image potential in a metal surface. *Phys. Rev. B* **34**, 6767 (1986).

60. Verzijl, C., Seldenthuis, J. & Thijssen, J. Applicability of the wide-band limit in DFT-based molecular transport calculations. *J. Chem. Phys.* **138**, 094102 (2013).

61. Nemec, N., Tománek, D. & Cuniberti, G. Contact dependence of carrier injection in carbon nanotubes: an ab initio study. *Phys. Rev. Lett.* **96**, 076802 (2006).

62. Covito, F., Eich, F., Tuovinen, R., Sentef, M. & Rubio, A. Transient charge and energy flow in the wide-band limit. *Journal of Chem. Theory Comput.* **14**, 2495–2504 (2018).

63. Zhu, Y., Maciejko, J., Ji, T., Guo, H. & Wang, J. Time-dependent quantum transport: direct analysis in the time domain. *Phys. Rev. B* **71**, 075317 (2005).

64. Guo, J., Datta, S., Lundstrom, M. & Anantam, M. Toward multiscale modeling of carbon nanotube transistors. *Int. J. Multiscale Comput. Eng.* **2**, 257–276 (2004).

65. Wu, T. & Guo, J. Multiscale modeling of semimetal contact to two-dimensional transition metal dichalcogenide semiconductor. *Appl. Phys. Lett.* **121**, 023507 (2022).

ACKNOWLEDGEMENTS

AUTHOR CONTRIBUTIONS

W.G.V. conceived the project. M.B. developed the code and performed the simulations. M.B., M.L.V. de.P., E.C., M.V.F., and W.G.V. analyzed the obtained results. M.B. wrote the paper with all the authors contributing to the discussion and preparation of the manuscript.

COMPETING INTERESTS

The authors declare no competing interests.

ADDITIONAL INFORMATION

Supplementary information The online version contains supplementary material available at https://doi.org/10.1038/s41699-023-00372-6.

Correspondence and requests for materials should be addressed to William G. Vandenberghe.

Reprints and permission information is available at http://www.nature.com/reprints

Publisher's note Springer Nature remains neutral with regard to jurisdictional claims in published maps and institutional affiliations.